Mechanical Deformation of Human Optic Nerve Head and Peripapillary Tissue in Response to Acute IOP Elevation

Yanhui Ma,[1] Elias Pavlatos,[1] Keyton Clayson,[1,2] Xueliang Pan,[3] Sunny Kwok,[1] Thomas Sandwisch,[1] and Jun Liu[1,2,4]

[1]Department of Biomedical Engineering, Ohio State University, Columbus, Ohio, United States
[2]Biophysics Interdisciplinary Group, Ohio State University, Columbus, Ohio, United States
[3]Department of Biomedical Informatics, Ohio State University, Columbus, Ohio, United States
[4]Department of Ophthalmology and Visual Science, Ohio State University, Columbus, Ohio, United States

PURPOSE. To measure the deformation of the human optic nerve head (ONH) and peripapillary tissue (PPT) in response to acute intraocular pressure (IOP) elevation.

METHODS. The ONH and PPT of 14 human donor globes were imaged with high-frequency ultrasonography during inflation testing from 5 to 30 mm Hg. A correlation-based speckle tracking algorithm was used to compute tissue displacements, and the through-thickness, in-plane, and shear strains were calculated by using least-squares strain estimation methods. The ONH and PPT were segmented along the anterior-posterior direction and the nasal-temporal direction. Regional displacements and strains were analyzed and compared.

RESULTS. The ONH displaced more posteriorly than the PPT in response to an acute IOP increase. Scleral canal expansion was minimal but correlated with ONH posterior displacement at all IOP levels. Through-thickness compression was concentrated in the anterior of both the ONH and the PPT. Shear was concentrated in the vicinity of the canal with higher shear in the peripheral ONH than the central ONH and higher shear in the PPT near the scleral canal than that further away from the canal.

CONCLUSIONS. High-resolution ultrasound speckle tracking showed a displacement mismatch between the ONH and the PPT, larger compressive strains in the direction of IOP loading in the anterior ONH and PPT, and higher shear strains in the periphery of ONH in response to acute IOP elevation in the human eye. These findings delineate the deformation patterns within and around the ONH and may help understand IOP-associated optic nerve damage.

Keywords: glaucoma, biomechanics, ultrasound, optic nerve head, peripapillary tissue

Glaucoma is associated with optic nerve damage and irreversible blindness. Evidence suggests that glaucomatous damage initiates within the optic nerve head (ONH),[1,2] which occupies a discontinuity in the posterior scleral shell where the retinal ganglion cell axons exit the eye. High intraocular pressure (IOP) is known to be one of the primary risk factors for glaucoma onset and progression, yet the mechanism linking IOP to glaucoma risk is not well understood. Elevation of IOP results in mechanical stresses and strains within the ONH that may be directly responsible for axonal injury or activate detrimental cellular responses[3,4] and extracellular matrix remodeling.[5,6] It is thus important to characterize the mechanical environment in the posterior eye during IOP elevation.

Recent years have seen important developments in the ability to directly measure ONH deformation, using various imaging modalities including histomorphometry,[7] confocal microscopy,[8] optical coherence tomography,[9,10] microcomputed tomography,[11] and second-harmonic generation imaging.[12,13] High-resolution images can be generated by using these techniques, but tissue penetration depth and/or displacement resolution are often limited. It remains unclear how tissue deformation may vary across the depth and width of the ONH and how the spatial variations in mechanical insults may relate to regional axonal damage. Our laboratory has developed a high-frequency ultrasound speckle tracking technique that overcomes the limitations and offers a better opportunity to delineate the complex mechanical responses of the different regions within and around the ONH.

High-frequency ultrasound imaging at 50 to 55 MHz has a unique combination of field of view (up to 10 mm), penetration depth (1–2 mm), and spatial resolution (10's of micrometers) that is suitable for simultaneous measurement of the ONH and the peripapillary tissue (PPT) through the entire tissue depth. Although high-frequency ultrasonography's advantage in tissue penetration depth over optical imaging comes with a trade-off in spatial resolution (ultrasonography: 10's of micrometers; optical imaging: a few micrometers), high-frequency ultrasound speckle tracking can achieve very high displacement sensitivity approaching that of optical methods (i.e., at the submicrometer level).[14–17] This speckle tracking method uses densely sampled radiofrequency (RF) data that preserve phase information to achieve displacement sensitivity and accuracy much higher than the spatial resolution of the imaging system. Others have reported achieving a vertical (i.e., the direction of sound propagation) displacement accuracy of 0.63 to 0.73 μm, using an ultrasound system at a frequency of 7.5 MHz.[18] Higher frequencies such as those used in our studies can achieve even

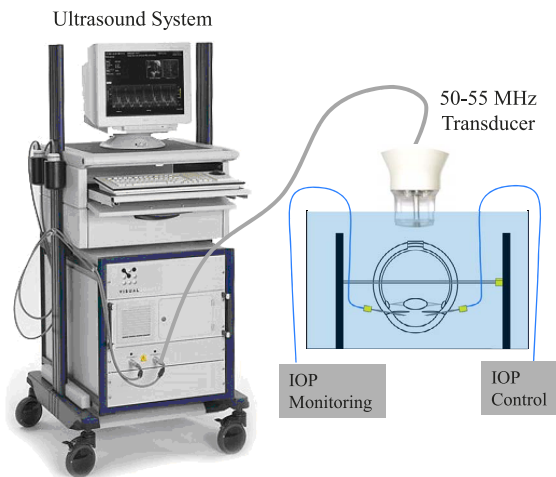Investigative Ophthalmology & Visual Science

FIGURE 1. Experimental setup used for inflation testing of human donor globes with ultrasound imaging of the ONH and PPT. Eye holder was immersed in saline.

higher displacement accuracy (at tens of nanometers) with interpolation.[19] Our previous studies[20] have reported an accuracy of less than 10% error for a 0.5 μm vertical displacement, using correlation-based high-frequency ultrasound speckle tracking (center frequency = 55 MHz). This technique detects strains down to 0.01% vertically and 0.025% horizontally (i.e., the direction perpendicular to sound propagation) with an error less than 10%.[20]

Using this high-resolution ultrasound speckle tracking technique, we aimed to image the full thickness of the human ONH and the surrounding PPT and quantify the regional mechanical deformation in response to IOP elevation.

METHODS

Donor Information and Experimental Setup

Fourteen human donor globes were obtained from the Lion's Eye Bank of West Central Ohio (Dayton, OH, USA) in accordance with the Declaration of Helsinki (age: 20–75 years; mean ± SD: 44 ± 17 years; 12 Caucasian and 2 African American; 9 male and 5 female). None of the donors had documented ocular diseases or surgeries. All globes were recovered within 12 hours postmortem and all experiments were completed within 36 hours postmortem. The globes were stored in a moist container at 4°C until experimental use.

The extraocular tissues were removed and the optic nerve was trimmed to be flush with the sclera. Whole globes were mounted in a custom-built holder with the ONH facing upward. Two spinal needles were inserted near the equator of the globe to secure the eye to the holder (Fig. 1). Two 20G needles were inserted into the anterior chamber of the eye, one connected to a programmable syringe pump (PhD Ultra; Harvard Apparatus, Holliston, MA, USA) to control IOP, and the other connected to a pressure sensor (P75; Harvard Apparatus) to continuously record IOP. The eye was immersed in 0.9% saline to maintain tissue hydration and facilitate ultrasound transduction.

Inflation Testing With Ultrasound Scans

For all inflation testing, control of the testing apparatus and data acquisition were implemented by using a customized LabView program (National Instruments, Austin, TX, USA). The

globes were first preconditioned with 20 IOP cycles from 5 to 30 mm Hg before equilibrating at 5 mm Hg for 30 minutes. The inflation tests were then performed by increasing IOP from 5 to 30 mm Hg with 0.5 mm Hg steps. The IOP was held constant at each IOP level for 30 seconds before ultrasound scans were acquired. Seven donor globes were scanned by using the ultrasound probe RMV55 (Vevo 660; VisualSonics, Inc., Toronto, Ontario, Canada) and seven additional globes were scanned by using the ultrasound probe MS700 (Vevo 2100; VisualSonics, Inc.). It is noted that these two ultrasound imaging systems gave similar displacement and strain measurements and the results were thus combined for analyses. Cross-sectional images were acquired along the nasal-temporal meridian of the ONH with an image width of 8 mm.

Ultrasound Speckle Tracking

The ultrasound speckle tracking algorithms have been described and validated previously.[14,15] In brief, RF data, the digitized voltage values of the received ultrasound signal, are acquired during image acquisition. The RF data are stored as A-lines acquired at 19 μm intervals in the direction perpendicular to sound propagation (horizontal). The A-lines are sampled at approximately 1.5 μm in the direction of ultrasound wave propagation (vertical). Speckle tracking is performed by first defining the region of interest in the reference RF data obtained at the initial IOP. Within this region, the RF data are divided into kernels, each containing 51×31 pixels (vertical $\times$ horizontal), or approximately 75 μm $\times$ 570 μm in size. The kernels are overlapped by 50% to improve spatial resolution of the strain image.[14] To compute the displacements of each kernel, a cross-correlation approach is used to evaluate the similarity of the kernels in successive images within a search window. The maximum correlation coefficient value designates the new location of the kernel, and spline interpolation allows for subpixel resolution in displacement tracking. Cumulative displacements are used to calculate kernel displacement with respect to its location at the initial IOP. The strains are calculated from the displacement field by using least-squares strain estimation.[21] A coordinate transformation converts the strains from Cartesian coordinates to the directions perpendicular and parallel to the tissue curvature (i.e., through-thickness and in-plane). Change in the size of the scleral canal was calculated in the scanned nasal-temporal meridian as the difference in the horizontal displacements between the PPT on either side of the ONH. The displacements and strains were analyzed from ultrasound data separated by 2.5 mm Hg intervals. Color maps were generated to visualize the spatial distribution of the tissue displacements and strains.

Regional Comparison of Deformation

The ONH and PPT were manually delineated from differences in signal intensity in the reference ultrasound images, with the sclera having a distinctively brighter appearance than the tissues within the ONH. The ONH and PPT were further divided into two equal-thickness layers for comparison of the anterior and posterior regions for each tissue. The ONH was also segmented into central and peripheral regions by dividing it into equal horizontal thirds, and the PPT was segmented into two equal length regions: the "near PPT," which is close to the canal, and the "far PPT," which is further away from the canal. Three regional analyses were performed (Fig. 2):

1. A comparison of the ONH and PPT to identify their differences and correlations in their mechanical responses;
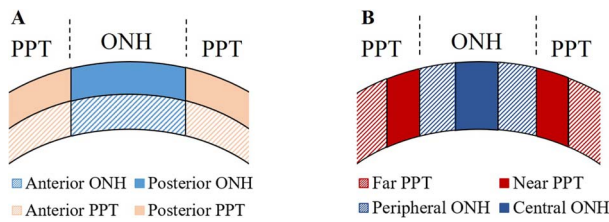
FIGURE 2. Divisions used for regional analyses of mechanical behavior. (**A**) The anterior and posterior halves of the ONH and PPT. (**B**) Divisions along the nasal-temporal direction within the ONH and PPT.

2. A comparison of the anterior and posterior regions of the ONH and between those two regions of the PPT to quantify depth-dependent changes in mechanical behavior; and

3. A comparison of the central and peripheral regions of the ONH, and the near and far regions of the PPT, to delineate the mechanical responses at the transitional interface between PPT to ONH.

The displacements and strains were summarized by using mean and standard deviation at different IOP levels for each region of interest. While data at different IOP levels are shown in figures, only data at 30 mm Hg are reported in the text as an example. The differences and correlations of the average strains between the different regions were evaluated by using paired *t*-tests and Pearson correlations at each preselected IOP level (10, 15, 20, 25, and 30 mm Hg). The *P* values were reported without multiple comparisons correction. To control the type I error for the multiple comparisons at different pressure levels, the Hochberg's step-up method was used.[22] Hochberg's step-up method declares that all tests are significant if the highest *P* values of these tests is less than 0.05, which is more powerful than the Bonferroni method or the Holm's procedure for multiple comparison adjustment. As a sensitivity analysis, linear mixed models for repeated measures (at selected IOP levels and different regions for each eye) were used to confirm the overall differences between regions. All data analysis was conducted by using SAS software (V9.4; SAS Institute Inc., Cary, NC, USA).

RESULTS

Color maps of vertical displacement, scleral canal expansion, and different types of strains for a representative human donor eye at 30 mm Hg are presented in Figure 3. Regional variation in displacements and strains was observed between and within the ONH and the PPT.

ONH Versus PPT Comparison

The posterior displacement of the ONH and PPT increased nonlinearly with increasing IOP, and displacement of the ONH was larger at every IOP level (all *P* < 0.001; Fig. 4A). Despite the mismatch in magnitude, the posterior displacements of the ONH and PPT were highly correlated with *R* > 0.92 at all IOP levels. The correlation between ONH and PPT displacement was in agreement with previous findings in porcine eyes, using the same experimental protocol, but the displacement magnitudes in human donor eyes were much smaller than those in porcine eyes (102.7 ± 41.7 μm versus 348.9 ± 82.2 μm for ONH and 58.9 ± 37.2 μm versus 219.7 ± 65.8 μm for PPT at 30 mm Hg; Fig. 4A).[23]

The average change in the width of the scleral canal in the nasal-temporal meridian remained minimal throughout the inflation test. Among the 14 tested donor eyes, the canal expansion ranged from 7.3 to 35.2 μm (19.5 ± 8.2 μm) at 30 mm Hg, much smaller than what was observed in porcine eyes (range, 76.6–163.5 μm; 127.7 ± 31.3 μm) for the same pressure rise (i.e., 5–30 mm Hg). In human donor eyes, the ONH posterior displacement was significantly larger in magnitude than canal expansion at every IOP level (all *P* < 0.001; Fig. 4B), and a correlation of *R* > 0.68 was found between ONH posterior displacement and canal expansion at all pressure levels. A larger posterior displacement than canal expansion was also observed in porcine eyes (Fig. 4B).[23]

Overall there was a relatively large negative through-thickness strain (indicating compression) in both the ONH and PPT (−1.63% ± 0.91% and −2.46% ± 1.00%, respectively, at 30 mm Hg) with an increasing magnitude as IOP increased (Fig. 5A). The average through-thickness strain was significantly larger in magnitude in the PPT than in the ONH at pressure levels above 10 mm Hg (*P* < 0.05; Fig. 5A). The in-plane tensile stretch was small on average in both ONH and PPT (Fig. 5B). At
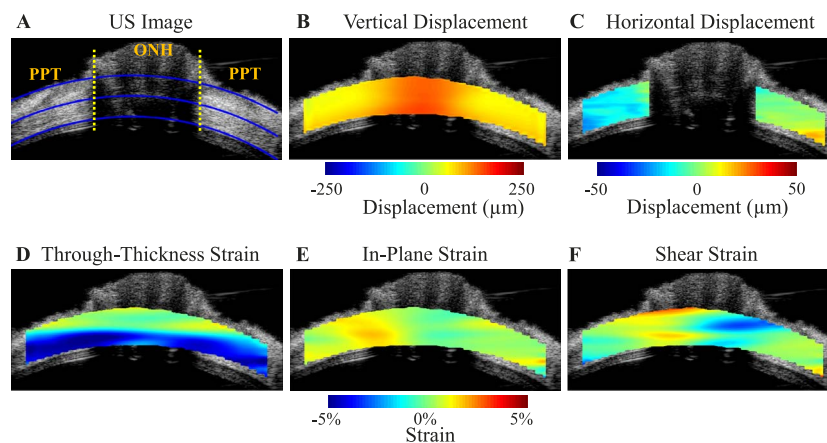

FIGURE 3. Ultrasound (US) image (**A**) and color maps of vertical displacement (**B**), scleral canal expansion (**C**), and strains (**D–F**) for a representative human donor eye at 30 mm Hg. The *yellow dotted lines* in (**A**) indicate the boundaries between ONH and PPT, the *inner* and *outer blue lines* are fitted curves for demarcation of region of interest (ROI) for strain analysis, and the *middle blue line* is used to divide the anterior and posterior halves. Note that the retina is largely excluded from the ROI. Positive displacements = upward vertical movement or rightward horizontal movement. Vertical displacements were larger within the ONH. The horizontal displacement of PPT was negative on average on the left side of ONH and positive on the right side of ONH, indicating a small scleral canal expansion. Through-thickness compression was largest in magnitude and concentrated in the anterior half of the ONH and PPT.
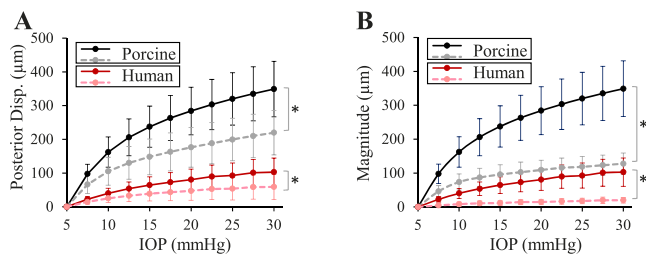
FIGURE 4. (**A**) Posterior displacement of the ONH (*solid lines*) and PPT (*dashed lines*) in human donor eyes ($n = 14$) and porcine eyes ($n = 12$), and (**B**) posterior displacement of the ONH (*solid lines*) and scleral canal expansion (*dashed lines*) in human donor eyes ($n = 14$) and porcine eyes ($n = 12$). *Asterisk* (*) indicates statistical significance ($P < 0.05$) in paired *t*-tests at 30 mm Hg.

30 mm Hg, the average in-plane strains in the ONH and PPT were 0.40% ± 0.26% and 0.63% ± 0.25%, respectively. The average shear strains had similar magnitudes in the ONH and the PPT at every IOP level (1.08% ± 0.38% and 1.07% ± 0.63%, respectively, at 30 mm Hg; Fig. 5C).

Anterior-Posterior Variation

All tested eyes exhibited substantial depth-dependent deformation in both the ONH and the PPT (Fig. 3). The through-thickness strain was significantly larger in the anterior layer than the posterior for both the ONH and PPT ($P < 0.05$ for IOP levels above 10 mm Hg; Figs. 6A, 6D). Within the ONH, the in-plane strain was significantly larger in the anterior layer than the posterior ($P < 0.05$ for IOP levels above 15 mm Hg; Fig. 6B), whereas in the PPT the in-plane strain was not different between the layers (all $P > 0.05$; Fig. 6D). Shear strain in the ONH showed no significant difference between anterior and posterior layers (all $P > 0.05$; Fig. 6E), whereas in PPT it was slightly larger in the posterior layer ($P < 0.05$ for IOP levels above 15 mm Hg; Fig. 6F). Through-thickness compression in the anterior layer was the largest strain in magnitude (3.20% ± 1.50% in ONH and 3.52% ± 1.22% in PPT at 30 mm Hg; see Table 1). A correlation of $R > 0.6$ was found between the anterior and posterior ONH in-plane strains at every IOP level except for 30 mm Hg (Table 2) and the correlation coefficient decreased with increasing IOP. A correlation of $R > 0.8$ was found for shear strains between the anterior and posterior PPT at all IOP levels (Table 2).

Central-Peripheral Variation

Within the ONH, both in-plane and shear strains were significantly higher in the periphery than the center at every IOP level (all $P < 0.05$; Figs. 7B, 7C). The ONH through-thickness strain was not different between central and peripheral ONH (all $P > 0.05$; Fig. 7A). A correlation of $R >$ 0.6 was found at all IOP levels for all three types of strains between the central and peripheral ONH regions.

In the PPT, the in-plane and shear strains were significantly higher in the region close to the scleral canal (the "near PPT") than in the region away from the canal (the "far PPT") (all $P < 0.05$, Fig. 7E; $P < 0.05$ for IOP levels above 15 mm Hg, Fig. 7F). The far region showed larger compressive through-thickness strains than the near region ($P < 0.05$ for IOP levels above 20 mm Hg; Fig. 7D). A correlation of $R > 0.8$ was found between the near and far PPT regions at all IOP levels for through-thickness and shear strains (Table 2).

DISCUSSION

In this study, high-frequency ultrasound speckle tracking was used to measure the mechanical responses of the human posterior eye to IOP elevation. With the advantages of high resolution, adequate penetration depth, and a wide field of view, we were able to acquire full-thickness and simultaneous measurements of human ONH and PPT deformation during whole eye inflation. This approach allowed for analyses of the depth-dependent and regional variations of the deformation within and around the ONH where glaucoma-related damages initiate. Such analyses provide us with new insights into the complex mechanical responses and interactions at the ONH during IOP change, beyond what was previously possible with optical imaging or histology. The primary findings of this study are as follows:

1. The ONH displaced more posteriorly than the PPT in response to an acute IOP increase in all tested human donor eyes (Fig. 4A). Despite the difference, the posterior displacements of these two regions were highly correlated.
2. There was a minimal expansion of the scleral canal in all tested eyes (on average approximately 20 μm) when IOP was raised from 5 to 30 mm Hg (Fig. 4B). There was also a minimal in-plane stretch within the ONH (on average 0.40%) relative to the through-thickness and shear strains. Canal expansion was correlated with ONH posterior displacement at all IOP levels.
3. Through-thickness compressive strains but not shear strains were highly concentrated in the anterior of both the ONH and the PPT in all tested eyes (Fig. 8A).
4. The largest shear was concentrated in the vicinity of the conjunction between ONH and PPT, with higher shear in the peripheral ONH than the central ONH and higher shear in the PPT near the scleral canal than that further away from the canal (Fig. 8B).

We have previously reported several similar findings in porcine eyes,[23] including a correlated but larger posterior displacement of the ONH as compared to the surrounding scleral tissue; a smaller magnitude of canal expansion in comparison to the ONH posterior displacement; and anterior
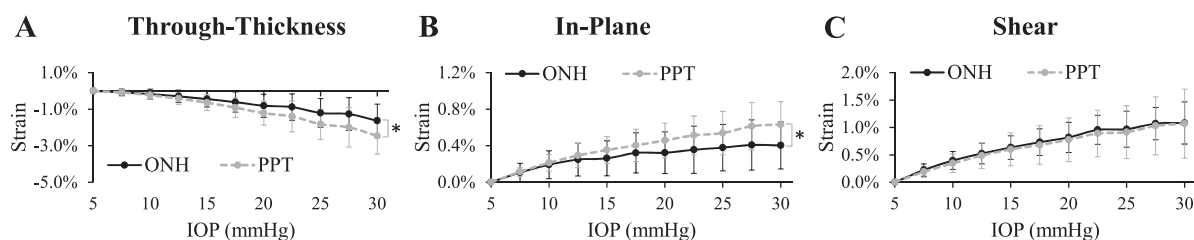

FIGURE 5. (**A**) Through-thickness, (**B**) in-plane, and (**C**) shear strains in the human ONH and PPT during inflation ($n = 14$). *Asterisk* indicates statistical significance ($P < 0.05$) in paired *t*-tests at 30 mm Hg.
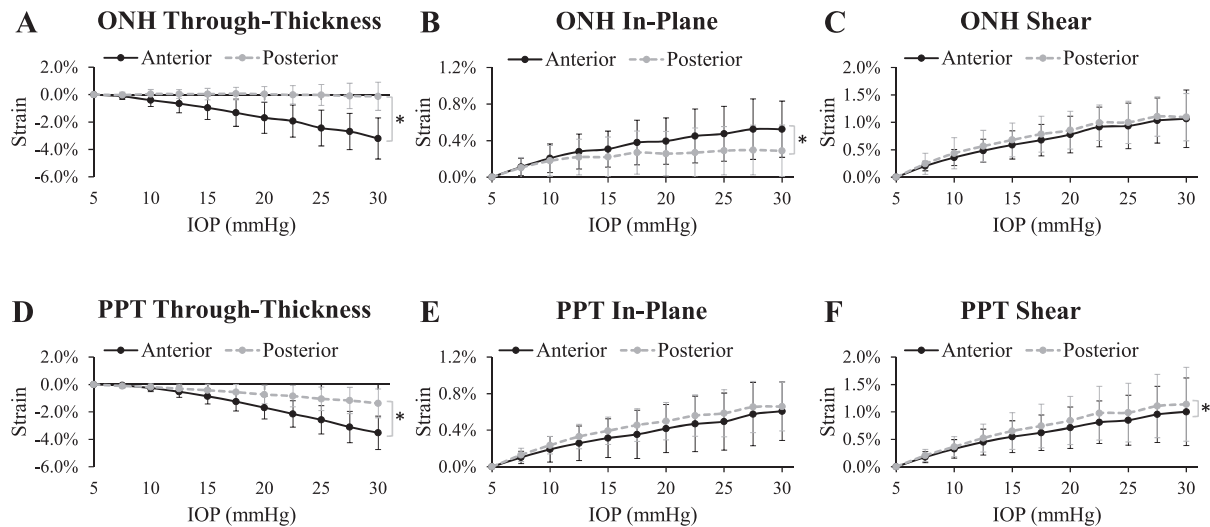
FIGURE 6. Average strains in the anterior and posterior regions of the ONH (**A–C**) and PPT (**D–F**). *Asterisk* indicates statistical significance ($P < 0.05$) in paired *t*-tests at 30 mm Hg.

concentration of through-thickness compression and peripheral concentration of shear strain within the ONH. In the present study, we observed several interesting differences between the human and porcine eye. First, the magnitudes of the posterior displacements and canal expansion were much smaller in the human eye than the porcine eye (ONH posterior displacement: 102.7 ± 41.7 μm versus 348.9 ± 82.2 μm; canal expansion: 19.5 ± 8.2 μm versus 127.7 ± 31.3 μm, at 30 mm Hg). The larger deformation seen in the porcine eye was likely due to its more compliant extracellular matrix with lower resistance to IOP.[24,25] Second, both through-thickness and shear strains were concentrated in the anterior porcine ONH, but in the human eye, only through-thickness strain was concentrated in the anterior ONH, while large shear strain appeared at various depths within the ONH. The difference in the location of shear concentration might be related to the difference in the location of lamina cribrosa (LC). In the porcine eye, the LC is located within the anterior ONH. In humans, LC insertion can vary substantially through depth.[26] Future studies are needed to corroborate this finding. Third, the in-plane strain observed within the human ONH was approximately an order of magnitude smaller than that in the porcine ONH ($0.40\% \pm 0.26\%$ vs. $3.63\% \pm 1.40\%$, at 30 mm Hg). It is unclear if this is solely due to the much stiffer tissue in the human posterior eye, particularly that of the scleral

collagen annulus as discussed later. It is noted that the human ONH has an irregular shape[27] and other cross-sections of the ONH might show different levels of in-plane stretch. Nonetheless, our results suggested that the in-plane stretch likely is not a dominant deformation mode in the human ONH in response to acute pressure rise.

One prominent feature of the through-thickness strain was the much larger magnitude in the anterior ONH and PPT (Figs. 6A, 6D). Anatomically, the anterior ONH contains the prelaminar neural tissue, while the anterior PPT contains the choroid. The presence of these tissues may underlie the larger through-thickness compressive strains in the anterior region. Future studies are needed to investigate whether and how the large compressive strains in the anterior ONH may affect axonal transport and astrocyte mechanotransduction in this region. The choroidal tissue may likely have a different mechanical response under the in vivo condition with blood filling in the capillary beds. Girard et al.[9] have used Optical Coherence Tomography to measure the mechanical response of the human posterior eye in vivo before and after IOP-lowering trabeculectomy and reported higher compressive strain relief in the peripapillary sclera and choroid than the LC or prelaminar neural tissue. This result is in principle consistent with our finding that a larger through-thickness strain was measured in the PPT than the ONH during pressure rise (Fig. 5A).

Our results showed minimal in-plane strain within the ONH, which was somewhat contrary to what was predicted by

TABLE 1. Average Regional Strains at 30 mm Hg in the ONH and PPT of All Donor Eyes ($n = 14$).

Strain (at 30 mm Hg)	Through-Thickness, Mean ± SD, %	In-Plane, Mean ± SD, %	Shear, Mean ± SD, %
ONH	−1.63 ± 0.91	0.40 ± 0.26	1.08 ± 0.38
PPT	−2.46 ± 1.00	0.63 ± 0.25	1.07 ± 0.63
Anterior ONH	−3.20 ± 1.50	0.52 ± 0.31	1.06 ± 0.52
Posterior ONH	−0.13 ± 1.03	0.29 ± 0.28	1.09 ± 0.43
Anterior PPT	−3.52 ± 1.22	0.61 ± 0.32	1.00 ± 0.62
Posterior PPT	−1.38 ± 1.05	0.66 ± 0.27	1.14 ± 0.67
Central ONH	−1.52 ± 0.90	0.22 ± 0.31	0.78 ± 0.39
Peripheral ONH	−1.70 ± 0.95	0.50 ± 0.26	1.25 ± 0.45
Near PPT	−2.25 ± 1.02	0.70 ± 0.26	1.14 ± 0.70
Far PPT	−2.85 ± 1.07	0.52 ± 0.33	0.94 ± 0.52

TABLE 2. Pearson Correlation Coefficients ($n = 14$) Between Different Regions for Through-Thickness, In-Plane, and Shear Strains at 30 mm Hg

Pearson Correlation R (at 30 mm Hg)	Through-Thickness Strain	In-Plane Strain	Shear Strain
ONH versus PPT	0.74*	0.43	0.64*
Anterior versus posterior ONH	0.03	0.53	0.29
Anterior versus posterior PPT	0.59*	0.48	0.92*
Central versus peripheral ONH	0.90*	0.75*	0.64*
Near versus far PPT	0.81*	0.57*	0.95*

* Significant correlation at 0.05 significance level. It is noted that the current sample size provides 80% power to detect correlations larger than 0.61, based on one-sided test.
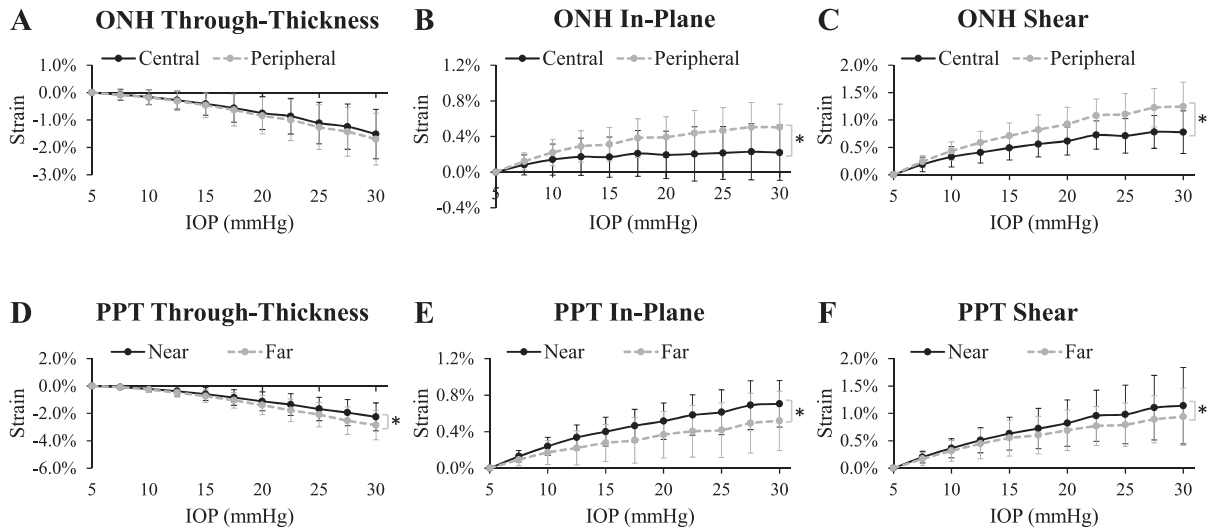
FIGURE 7. Average strains in the central and peripheral regions of the ONH (**A–C**), and the near and far regions of the PPT (**D–F**). *Asterisk* indicates statistical significance ($P < 0.05$) in paired *t*-tests at 30 mm Hg.

computational models that did not include a collagen annulus ring around the scleral canal in the peripapillary sclera and predicted large membrane tensile deformation within LC.[28] On the other hand, computational models incorporating the annulus ring predicted small in-plane tensile stretch but significant posterior bending of the LC during pressure rise.[29,30] Our experimental findings showed a 2-fold higher shear than the in-plane strain within human ONH, consistent with the predictions made from models incorporating the collagen annulus ring.

Shear strains appeared to concentrate at the conjunction of the ONH and PPT, presumably owing to the transition of tissue material properties in this region. This was shown by the higher strains in the peripheral ONH and the PPT close to the scleral canal. A recent study[13] has reported a higher in-plane shear strain in the periphery than the central region of the LC. It is noted that the shear strain reported in the present study was in the plane perpendicular to the curvature of sclera/LC. As described earlier, the ONH displaces more posteriorly than the PPT (Fig. 4A) and the difference in posterior displacement between these two regions leads to a bending deformation in the transition region. We calculated the overall difference in the average posterior displacement between these two regions, namely, the displacement mismatch. Our data showed that ONH peripheral shear may be correlated with the displacement mismatch ($R = 0.58$ at 30 mm Hg), suggesting that the displacement mismatch between the ONH and the

PPT may be the primary factor underlying the out-of-plane shear in the peripheral ONH.

The substantially higher shear at the peripheral ONH may underlie the higher susceptibility of the peripheral optic nerve axon bundles characteristic to glaucoma. This may also be associated with LC defects frequently observed in glaucomatous eyes, such as tear and disinsertion.[31,32] Optic disc hemorrhage has been recognized as an important marker for glaucoma progression[33] and may precede changes in retinal nerve fiber layer and visual fields. Our study showed that shear strain was concentrated in the vicinity of the canal border where disc hemorrhage often occurs, suggesting a potential link between increased shear and disc hemorrhage, as shearing forces in the peripapillary sclera may damage the small arteries residing in this region including the branches of the posterior ciliary arteries and the circle of Zinn-Haller.

This study had a few limitations. First, the ex vivo experimental condition and tissue preparation may have resulted in alterations of the tissues as compared to in vivo. Among others, postmortem tissue degradation and swelling, trimming of the optic nerve, and the absence of cerebrospinal fluid and blood pressure could potentially have some significant effects. All experiments were completed within 36 hours of postmortem time, which is well within the recommended time window of 72 hours to avoid collagen degradation,[34] but it is unclear if neural tissue and cellular components were altered to the extent of affecting ONH mechanical responses. Trimming of the optic nerve was
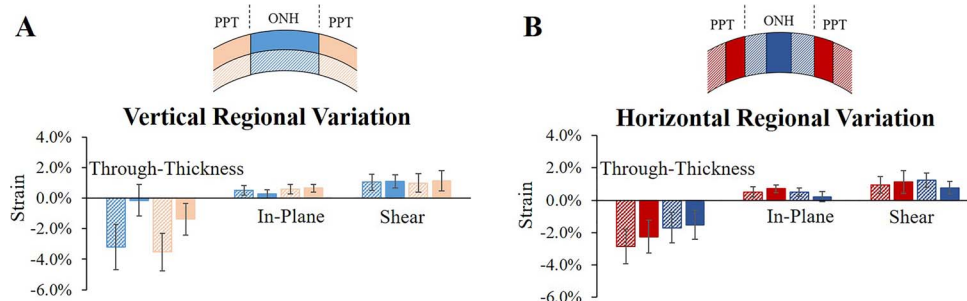

FIGURE 8. Regional strains of the PPT and the ONH at 30 mm Hg with divisions made (**A**) in the vertical direction (anterior and posterior) and (**B**) in the horizontal direction (far, near, peripheral, and central).

necessary for full-thickness imaging of the ONH but may have altered the boundary conditions of the posterior eye. Cerebrospinal fluid in the subarachnoid space of the optic nerve may exert a loading on the posterior eye and influence the deformation response to IOP elevation.[35–37] Blood pressure may also have an impact on IOP-related deformations,[38,39] particularly in the central ONH and the highly vascularized choroid. Secondly, the anatomic boundaries of structures such as the LC and choroid could not be clearly delineated from the ultrasound images of some eyes. Future efforts will be made to optimize image acquisition or coregister with histology to quantify responses of these specific anatomic regions. Third, the current 2D method does not provide the full 3D analysis of the different quadrants in the posterior eye. Previous 3D histomorphology studies[40] have shown regional variance in the shape and thickness of sclera flange and lamina cribrosa in nonhuman primates. Regional strain analysis of the peripapillary sclera showed higher strains in the inferotemporal sector of human posterior sclera,[41] which might underline higher rates of damage in certain quandrants.[42] Future studies will aim to acquire 3D scans of the mechanical response of the ONH and PPT to better delineate their complex regional variances in deformation.

In conclusion, high-resolution ultrasound speckle tracking was used to simultaneously measure the mechanical responses of the human ONH and PPT to IOP elevation. Primary findings included a larger ONH displacement in the anterior-posterior direction than in the surrounding PPT, higher compressive strain in the direction of IOP loading in the anterior ONH and PPT, and higher shear strain in the periphery of the ONH. These findings of IOP-related mechanical behavior of the posterior eye may provide new insights to better understand the biomechanical factors associated with extracellular matrix remodeling and axonal damage in glaucoma.

References

1. Quigley HA, Addicks EM, Green WR, Maumenee AE. Optic nerve damage in human glaucoma, II: the site of injury and susceptibility to damage. *Arch Ophthalmol*. 1981;99:635–649.

2. Nickells RW, Howell GR, Soto I, John SWM. Under pressure: cellular and molecular responses during glaucoma, a common neurodegeneration with axonopathy. *Annu Rev Neurosci*. 2012;35:153–179.

3. Hernandez MR, Miao H, Lukas T. Astrocytes in glaucomatous optic neuropathy. *Prog Brain Res*. 2008;173:353–373.

4. Wang R, Seifert P, Jakobs TC. Astrocytes in the optic nerve head of glaucomatous mice display a characteristic reactive phenotype. *Invest Ophthalmol Vis Sci*. 2017;58:924–932.

5. Downs JC, Roberts MD, Sigal IA. Glaucomatous cupping of the lamina cribrosa: a review of the evidence for active progressive remodeling as a mechanism. *Exp Eye Res*. 2011; 93:133–140.

6. Hernandez MR. Ultrastructural immunocytochemical analysis of elastin in the human lamina cribrosa: changes in elastic fibers in primary open-angle glaucoma. *Invest Ophthalmol Vis Sci*. 1992;33:2891–2903.

7. Yang H, Downs JC, Sigal IA, Roberts MD, Thompson H, Burgoyne CF. Deformation of the normal monkey optic nerve head connective tissue after acute IOP elevation within 3-D histomorphometric reconstructions. *Invest Ophthalmol Vis Sci*. 2009;50:5785–5799.

8. Albon J, Purslow PP, Karwatowski WSS, Easty DL. Age related compliance of the lamina cribrosa in human eyes. *Br J Ophthalmol*. 2000;84:318–323.

9. Girard MJA, Beotra MR, Chin KS, et al. In vivo 3-dimensional strain mapping of the optic nerve head following intraocular pressure lowering by trabeculectomy. *Ophthalmology*. 2016; 123:1190–1200.

10. Fazio MA, Clark ME, Bruno L, Girkin CA. In vivo optic nerve head mechanical response to intraocular and cerebrospinal fluid pressure: imaging protocol and quantification method. *Sci Rep*. 2018;8:12639.

11. Coudrillier B, Geraldes DM, Vo NT, et al. Phase-contrast micro-computed tomography measurements of the intraocular pressure-induced deformation of the porcine lamina cribrosa. *IEEE Trans Med Imaging*. 2016;35:988–999.

12. Sigal IA, Grimm JL, Jan N-J, Reid K, Minckler DS, Brown DJ. Eye-specific IOP-induced displacements and deformations of human lamina cribrosa. *Invest Ophthalmol Vis Sci*. 2014;55: 1–15.

13. Midgett DE, Pease ME, Jefferys JL, et al. The pressure-induced deformation response of the human lamina cribrosa: analysis of regional variations. *Acta Biomater*. 2017;53:123–139.

14. Tang J, Liu J. Ultrasonic measurement of scleral cross-sectional strains during elevations of intraocular pressure: method validation and initial results in posterior porcine sclera. *J Biomech Eng*. 2012;134:91007.

15. Cruz Perez B, Pavlatos E, Morris HJ, et al. Mapping 3D strains with ultrasound speckle tracking: method validation and initial results in porcine scleral inflation. *Ann Biomed Eng*. 2016;44:2302–2312.

16. Clayson K, Pavlatos E, Ma Y, Liu J. 3D Characterization of corneal deformation using ultrasound speckle tracking. *J Innov Opt Health Sci*. 2017;10:1742005.

17. Palko JR, Tang J, Cruz Perez B, Pan X, Liu J. Spatially heterogeneous corneal mechanical responses before and after riboflavin—ultraviolet-A crosslinking. *J Cataract Refract Surg*. 2014;40:1021–1031.

18. Hansen HHG, Lopata RGP, Idzenga T, de Korte CL. Full 2D displacement vector and strain tensor estimation for superficial tissue using beam-steered ultrasound imaging. *Phys Med Biol*. 2010;55:3201–3218.

19. Akyildiz AC, Hansen HHG, Nieuwstadt HA, et al. A framework for local mechanical characterization of atherosclerotic plaques: combination of ultrasound displacement imaging and inverse finite element analysis. *Ann Biomed Eng*. 2016; 44:968–979.

20. Pavlatos E, Chen H, Clayson K, Pan X, Liu J. Imaging corneal biomechanical responses to ocular pulse using high-frequency ultrasound. *IEEE Trans Med Imaging*. 2018;37:663–670.

21. Kallel F, Ophir J. A least-squares strain estimator for elastography. *Ultrason Imaging*. 1997;19:195–208.

22. Huang Y, Hsu JC. Hochberg's step-up method: cutting corners off Holm's step-down method. *Biometrika*. 2007;94:965–975.

23. Pavlatos E, Ma Y, Clayson K, Pan X, Liu J. Regional deformation of the optic nerve head and peripapillary sclera during IOP elevation. *Invest Ophthalmol Vis Sci*. 2018;59: 3779–3788.

24. Cruz Perez B, Tang J, Morris HJ, et al. Biaxial mechanical testing of posterior sclera using high-resolution ultrasound speckle tracking for strain measurements. *J Biomech*. 2014; 47:1151–1156.

25. Wollensak G, Spoerl E. Collagen crosslinking of human and porcine sclera. *J Cataract Refract Surg*. 2004;30:689–695.

26. Girkin CA, Fazio MA, Yang H, et al. Variation in the three-dimensional histomorphometry of the normal human optic

nerve head with age and race: lamina cribrosa and peripapillary scleral thickness and position. *Invest Ophthalmol Vis Sci*. 2017;58:3759–3769.

27. Sanfilippo PG, Cardini A, Hewitt AW, Crowston JG, Mackey DA. Optic disc morphology—rethinking shape. *Prog Retin Eye Res*. 2009;28:227–248.

28. Sigal IA, Yang H, Roberts MD, Burgoyne CF, Downs JC. IOP-induced lamina cribrosa displacement and scleral canal expansion: an analysis of factor interactions using parameterized eye-specific models. *Invest Ophthalmol Vis Sci*. 2011;52:1896–1907.

29. Girard MJA, Downs JC, Burgoyne CF, Suh J-KF. Peripapillary and posterior scleral mechanics—part I: development of an anisotropic hyperelastic constitutive model. *J Biomech Eng*. 2009;131:51011.

30. Grytz R, Meschke G, Jonas JB. The collagen fibril architecture in the lamina cribrosa and peripapillary sclera predicted by a computational remodeling approach. *Biomech Model Mechanobiol*. 2011;10:371–382.

31. Sharpe GP, Danthurebandara VM, Vianna JR, et al. Optic disc hemorrhages and laminar disinsertions in glaucoma. *Ophthalmology*. 2016;123:1949–1956.

32. You JY, Park SC, Su D, Teng CC, Liebmann JM, Ritch R. Focal lamina cribrosa defects associated with glaucomatous rim thinning and acquired pits. *JAMA Ophthalmol*. 2013;131:314–320.

33. Drance SM. Disc hemorrhages in the glaucomas. *Surv Ophthalmol*. 1989;33:331–337.

34. Girard M, Suh J-KF, Hart RT, Burgoyne CF, Downs JC. Effects of storage time on the mechanical properties of rabbit peripapillary sclera after enucleation. *Curr Eye Res*. 2007;32:465–470.

35. Berdahl JP, Allingham RR, Johnson DH. Cerebrospinal fluid pressure is decreased in primary open-angle glaucoma. *Ophthalmology*. 2008;115:763–768.

36. Hua Y, Voorhees AP, Sigal IA. Cerebrospinal fluid pressure: revisiting factors influencing optic nerve head biomechanics. *Invest Ophthalmol Vis Sci*. 2018;59:154–165.

37. Feola AJ, Coudrillier B, Mulvihill J, et al. Deformation of the lamina cribrosa and optic nerve due to changes in cerebrospinal fluid pressure. *Invest Ophthalmol Vis Sci*. 2017;58:2070–2078.

38. Flammer J, Orgül S, Costa VP, et al. The impact of ocular blood flow in glaucoma. *Prog Retin Eye Res*. 2002;21:359–393.

39. He Z, Vingrys AJ, Armitage JA, Bui BV. The role of blood pressure in glaucoma. *Clin Exp Optom*. 2011;94:133–149.

40. Yang H, Downs JC, Girkin C, et al. 3-D histomorphometry of the normal and early glaucomatous monkey optic nerve head: lamina cribrosa and peripapillary scleral position and thickness. *Invest Ophthalmol Vis Sci*. 2007;48:4597–4607.

41. Fazio MA, Grytz R, Bruno L, et al. Regional variations in mechanical strain in the posterior human sclera. *Invest Ophthalmol Vis Sci*. 2012;53:5326–5333.

42. See JLS, Nicolela MT, Chauhan BC. Rates of neuroretinal rim and peripapillary atrophy area change: a comparative study of glaucoma patients and normal controls. *Ophthalmology*. 2009;116:840–847.